

NJC

New Journal of Chemistry

A journal for new directions in chemistry

Accepted Manuscript

This article can be cited before page numbers have been issued, to do this please use: B. Albuquerque, G. J. Chacon, M. Nazarkovsky and J. Dupont, *New J. Chem.*, 2020, DOI: 10.1039/D0NJ02419H.



This is an Accepted Manuscript, which has been through the Royal Society of Chemistry peer review process and has been accepted for publication.

Accepted Manuscripts are published online shortly after acceptance, before technical editing, formatting and proof reading. Using this free service, authors can make their results available to the community, in citable form, before we publish the edited article. We will replace this Accepted Manuscript with the edited and formatted Advance Article as soon as it is available.

You can find more information about Accepted Manuscripts in the [Information for Authors](#).

Please note that technical editing may introduce minor changes to the text and/or graphics, which may alter content. The journal's standard [Terms & Conditions](#) and the [Ethical guidelines](#) still apply. In no event shall the Royal Society of Chemistry be held responsible for any errors or omissions in this Accepted Manuscript or any consequences arising from the use of any information it contains.

Rhodium nanoparticles impregnated on TiO₂: Strong morphological effects on hydrogen production

Brunno L. Albuquerque,*^a Gustavo Chacón,^a Michael Nazarkovsky^b and Jairton Dupont^a

- a. LAMOCA – Laboratory of Molecular Catalysis, Institute of Chemistry – Universidade Federal do Rio Grande do Sul. Av. Bento Gonçalves, 9500 Porto Alegre 91501-970 RS (Brazil).
- b. Pontifícia Universidade Católica de Rio de Janeiro, Rua Marquês de São Vicente, 225, Rio de Janeiro 22451-900 RJ (Brazil).

(*). Corresponding author: E-mail address: brunno.albuquerque@ufrgs.br

Abstract

The effect of the shape of rhodium nanoparticles impregnated on TiO₂ on photocatalytic hydrogen generation using methanol as sacrificial reagent has been investigated by using a simple home-made UV-LED light strips reactor to activate the catalyst surface. For rhodium nanocubes, the normalised rate of H₂ production was 22.4 mmol h⁻¹ m⁻² at 365 nm and 7.5 mmol h⁻¹ m⁻² at 400 nm. Normalised activity/surface area of the studied Rh nanoparticles showed a trend that led to establishing a relationship between the exposed [100] facets and photocatalytic activity. The Rh shape-dependent H₂ production follows a trend of cubic > spherical > octahedral, which is associated with a higher surface energy of the Rh nanoparticles.

Introduction

The process of photocatalytic hydrogen production using TiO₂ as a catalyst and Pt as co-catalyst under UV irradiation was reported almost half a century ago.^{1,2} Since then, huge efforts have been dedicated to the development of new materials capable of being activated with the visible region of the solar spectrum for a diverse set of applications such as hydrogen production,³⁻⁵ CO₂ reduction,⁶⁻⁸ and decomposition of organic dyes,⁹⁻¹¹ amongst others. The emission of the solar spectrum in the UV region

1
2
3 accounts for only about 3-4% of all the light that reaches the Earth's surface.¹² However, the advent of
4
5 newer technologies of light-emitting diodes (LED) allows for the use of common photovoltaic cells and
6
7 hence, UV absorbing semiconductors can be used without modification to harvest photons in the visible
8
9 region indirectly.^{13, 14}
10

11
12
13 Although there have been several investigations regarding the composition of the co-catalyst in
14
15 H₂ production,¹⁵⁻¹⁷ only a few specific studies about crystal morphology and nanoparticle shape vs
16
17 activity has been reported thus far.¹⁸⁻²³ With the recent development of shape-controlled synthesis of
18
19 nanocrystals,²⁴⁻²⁷ a new field for catalysis has been opened for a plethora of specific transformations.^{28,}
20
21 ²⁹ The effect of octahedral and cubic Pd nanoparticles impregnated on TiO₂ has been investigated on
22
23 water photolysis using various alcohols as sacrificial agents and showed that exposed Pd [111] facets
24
25 increased the heterojunction between metal and semiconductor, thus enhancing hydrogen production.³⁰
26
27 However, an overall higher trend for H₂ production was demonstrated to be directly related to the [100]
28
29 facets of cubic nanoparticles.³¹⁻³³ For Rh nanoparticles deposited over graphitic carbon (g-C₃N₄), there
30
31 is no size dependence for hydrogen production in aqueous methanol. It was hypothesized that metallic
32
33 Rh was essential for the removal of photogenerated electrons at the surface.³⁴ Additionally, studies on
34
35 the effect of the size of Rh nanoparticles on GaN:ZnO in a sulfuric acid solution for photocatalytic
36
37 water splitting, indicated that the activity of Rh@Cr₂O₃ core-shell nanoparticles (NPs) is dependent
38
39 upon the size of the Rh core.³⁵ It is known that upon variation of the size of the nanocrystal, the ratio of
40
41 atoms in the edges, corners, faces and vertices is not constant; hence the normalisation of the surface
42
43 atoms by using metallic nanoparticles should be corrected.³⁶
44
45
46

47
48 In this study, we report the development of Rh NPs with different shapes as co-catalysts in the
49
50 photocatalytic reforming of methanol for the production of hydrogen in aqueous media. Three different
51
52 Rh NPs shapes were studied (cuboctahedra RhNP, cubic RhNC and octahedral RhOh) to evaluate the
53
54 surface composition activity by using the magic numbers approach (Figure 1).³⁶ The catalysts were
55
56 characterized by standard techniques such as, electron microscopy, textural and electronic properties.
57
58 Also, it was developed the LED reactor lamp which permitted this study.
59
60

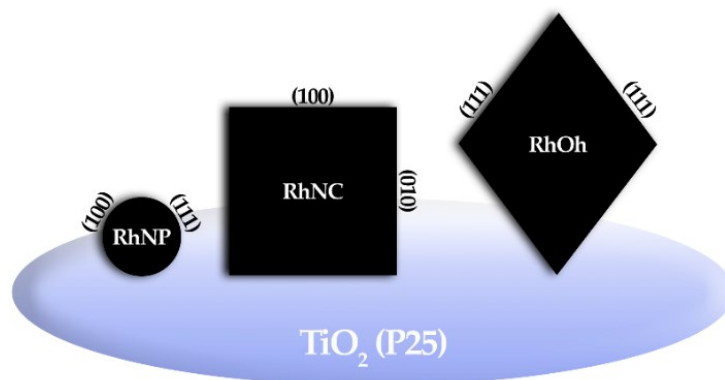


Figure 1. Illustration of Rh nanoparticles shapes used in this work showing the lattice planes of the exposed facets.³⁷

1. Experimental

1.1. Materials and methods

Rhodium chloride (RhCl_3) was purchased from Stream Chemicals, 2-bromoethanol was purchased from Oakwood Chemical China, TiO_2 aeroxide (P25) was obtained from Evonik Industries. 1-methyl imidazole was obtained from Spectrum Chemical and distilled under reduced pressure prior to use. Rhodium acetate dimer ($\text{Rh}_2(\text{OAc})_4$) and the other reagents were purchased from Sigma-Aldrich (Merck) and used without further purification. Methanol was HPLC grade and the deionized water (18.2 $\text{M}\Omega$ cm) were used throughout this study.

1.2. Reactor lamp design and reaction Schlenk vessel.

Two reactors were built by using 300-LED strips with emission at 365 ± 5 nm and 400 ± 10 nm. These strips were glued to the inner side of a cylinder ($\varnothing = 15$ cm, 15 cm height) were the top part was fitted with three small fans (60 mm) for forced ventilation (See Figure S1a, b for illustration). The power output of each strip is 20 W and 24 W, 365 nm and 400 nm, respectively. Both of the lamps were powered by the same 12 V, 20 amps power supply. The reaction vessel consisted on a Schlenk tube adapted with a GC septum for gas sampling as shown in Figure S1c.

1.2.1. Determination of UV-LED photon flux.

View Article Online
DOI: 10.1039/D0NJ02419H

The photon flux of the UV-LED reactor assembly was measured using the ferrioxalate actinometry adapted from the literature.³⁸ Three stock solutions were prepared using distilled water. The stock solution **A** was prepared by dissolution of 0.967 g of $\text{Fe}(\text{NO}_3)_3 \cdot 9\text{H}_2\text{O}$ (0.4 mol L^{-1}) in 10 mL of water. Oxalate stock solution **B** was prepared by dissolution of 2.0 g of $\text{K}_2\text{C}_2\text{O}_4$ (1.2 mol L^{-1}) in 10 mL of water. Stock solution **C** was prepared by dissolution of 10 mg of 1,10-phenantroline (5.5 mmol L^{-1}) and 2.245 g sodium bicarbonate (1.65 mol L^{-1}) in 10 mL of H_2O . Stock solutions **A** and **C** were protected from light.

The reaction solution was prepared by a mixture of 1.0 mL of solution **A** and **B**, diluted to 20 mL in darkness. Then, 10 mL of the reaction solution was transferred to the Schlenk tube used in the photocatalytic experiments equipped with a magnetic stirring bar and then irradiated for 5 min. After this time, 0.5 mL was taken from the reaction solution, mixed with 0.5 mL of stock solution **C** and diluted to 5 mL with H_2O . The spectrum was measured before and after the irradiation and the absorption at 510 nm used for quantification of Fe^{2+} formed. The photon flux was calculated by the formula:

$$n_{\text{Fe}^{2+}} = \frac{V_1 V_3 \Delta A}{V_2 l \varepsilon} \quad (1)$$

Were, V_1 is the volume of the irradiated solution (10 mL), V_2 is the volume taken from the reaction solution (0.5 mL) and V_3 is the volume measured in the UV-vis (5 mL). ΔA is the variation of maximum absorbance measured at 510 nm before and after the irradiation, l is the optical path length of the cuvette ($l = 1.0 \text{ cm}$) and ε is the molar extinction coefficient for $[\text{Fe}(\text{phen})]^{2+}$ ($11100 \text{ L}^{-1} \text{ mol}^{-1} \text{ cm}^{-1}$ at 510 nm). The number of incident photons is calculated by the formula:

$$\frac{n_{\text{photons}}}{\text{min}} = \frac{n_{\text{Fe}^{2+}}}{\phi_{\lambda} t F} \quad (2)$$

Were the quantum yield of Fe^{2+} production ($\Phi_{365} = 1.270$ and $\Phi_{400} = 1.188$)³⁹, t is the irradiation time (5 min) and F is the mean fraction of the absorbed light ($F = 1$).

1.3. Synthetic procedures

1.3.1. Synthesis of BMIm.OAc.

Previously, BMIm.Cl was prepared by reacting butyl chloride and 1-methylimidazole at 75-80 °C for 48 hours. After recrystallization in acetone/methanol mixture, BMIm.Cl was obtained as white crystals (yield: 80%). ¹H NMR (400 MHz, D₂O) δ ppm 0.89 (*t*, $J = 7.4$ Hz, 3H); 1.22–1.35 (*m*, 2H); 1.82 (*qp*, $J = 7.4$ Hz, 2H); 3.86 (*s*, 3H); 4.17 (*t*, $J = 7.2$ Hz, 2H); 7.40 (*d*, $J = 2.0$ Hz, 1H); 7.45 (*d*, $J = 2.0$, 1H). In a second step, the corresponding BMIm.OAc, was obtained by anion exchange using Amberlyst X resin saturated with OH⁻ ions. After the anion exchange, glacial acetic acid was added and the produced water removed by vacuum to obtain BMIm.OAc as a pale-yellow oil. Yield: 80%. NMR analysis. ¹H NMR (400 MHz, CDCl₃) δ ppm 0.97 (*t*, $J = 7.4$ Hz, 3H); 1.31–1.41 (*m*, 2H); 1.83-1.89 (*m*, 2H); 1.97 (*s*, 3H); 4.05 (*s*, 3H); 4.23 (*t*, $J = 7.4$ Hz, 2H); 7.24 (*s*, 1H); 7.30 (*s*, 1H); 11.08 (*s*, 1H). Residual water contents determined by Karl-Fischer titration (3%).

1.3.2. Synthesis of HEMIm.Br.

In a typical procedure, in a round bottomed flask equipped with a magnetic stirrer 10 mL of 1-methylimidazole (0.125 mol) and 10 mL of 2-bromoethanol (0.141 mol) were mixed at room temperature. After 48h the reaction flask was cooled until induce the precipitation of the HEMIm.Br. Then, resulting solid was washed with diethyl ether and dried over vacuum. Yield: 83 %, NMR analysis. ¹H NMR (400 MHz, D₂O) δ ppm; 3.80 (*s*, 1H); 3.84 (*m*, 2H); 4.64 (*s*, 2H); 7.35 (*t*, $J = 2.0$ Hz, 1H); 7.40 (*t*, $J = 2.0$, 1H).

1.3.3. Preparation of spherical Rhodium-impregnated TiO₂ (RhNP).

The RhNP were prepared by chemical reduction with NaBH₄. Typically, 8.0 mg of Rh₂(OAc)₄ (0.036 mmol in Rh) were dissolved in a solution containing 75.0 mg of BMIm.OAc (0.38 mmol) in 40

1
2
3 mL of deionized water. After 30 minutes under vigorous stirring, 10 mL of a freshly prepared ice-cold
4
5 NaBH_4 solution in deionized water (7.0 mg of NaBH_4 , 0.185 mmol) was added to the solution. After
6
7 few minutes, the initial blue colour turns to dark brown, characterizing the formation of the
8
9 Rh@BMIm.OAc .
10

11
12 The impregnation of Rh nanoparticles in TiO_2 procedure was adapted from literature.⁴⁰ In a
13
14 typical experiment, 1000 mg of TiO_2 (Evonik, P25) freshly macerated in an Agatha mortar were added
15
16 to a 50 mL of the Rh@BMIm.OAc colloidal solution under vigorous stirring during 48 hours. After this
17
18 time, RhNPs were isolated by centrifugation, washed with deionized water, and dried under vacuum at
19
20 60 °C for 12 hours. (Isolated yield: 917 mg.)
21
22

23 24 **1.3.4 Preparation of cubic Rhodium-impregnated TiO_2 (RhNC).**

25
26 The rhodium nanocubes were synthesized as follow: 42.0 mg of RhCl_3 (0.2 mmol), 444.5 mg
27
28 of PVP (55 Da, 4.0 mmol in monomer units) and 207.1 mg of HEMIm.Br (1.0 mmol) were placed in a
29
30 Schlenk tube and dissolved in ethylene glycol. This mixture was heated to 80 °C for 20 minutes under
31
32 vigorous stirring. After this time, the resulting solution was placed in a silicone bath at 185 °C and the
33
34 reaction conducted for 1.5 h. After this, acetone was added and the solution centrifuged to obtain a
35
36 precipitated that was re-dissolved with few drops of ethanol and acetone in order to remove remaining
37
38 PVP. RhNC were recovered by centrifugation and dried by vacuum (Isolated yield: 20.0 mg).
39
40
41

42
43 For impregnation of rhodium nanocubes in TiO_2 , 5.0 mg of previously isolated powder were
44
45 dissolved in 25 mL of water and added dropwise to a solution of 1000 mg TiO_2 in 25 mL of water. After
46
47 addition, the resulting solution was stirred for 48 h at room temperature, and RhNC isolated by
48
49 centrifugation. The RhNC were washed with deionized water, and dried under vacuum at 60 °C for 12
50
51 hours. (Isolated yield: 800 mg).
52
53

54 55 **1.3.5 Preparation of octahedral Rhodium-impregnated TiO_2 (RhOh).**

56
57 In a typical synthesis, PVP (55 Da, 33.3 mg, 0.29 mmol in monomer units), ascorbic acid (480
58
59 mg, 2.72 mmol) and citric acid (60 mg, 0.31 mmol) were dissolved in 9.0 mL of ethylene glycol under
60

magnetic stirring at 145 °C. In another flask, RhCl₃ (6.2 mg, 0.03 mmol) was totally dissolved in 20 mL of ethylene glycol and then added to the PVP, ascorbic acid and citric acid solution mixture. The reaction was carried out at 145 °C for 2 hours. After cooling to room temperature, the solution was centrifugated and washed with ethanol to remove the excess of PVP. Finally, the octahedral rhodium nanoparticles were isolated by centrifugation at 12000 RPM. (yield: 5 mg.) Same RhNC impregnation procedure was used for RhOh (Isolated yield: 740 mg)

1.4 Rh nanoparticles characterization.

The TEM samples were prepared by drop-casting the colloidal nanoparticles and the supported catalyst onto Cu grids (holey carbon – EMS), 300 mesh. The TEM images were acquired in a JEOL JEM 1011 electron microscope operating at 100 kV using at least 400k magnification. The HRTEM and HAADF-STEM images were acquired using a JEOL JEM 2100F electron microscope operated at 200 kV equipped with an Oxford Instruments X-Max^N 80 LTE EDS detector, which was used for elemental mapping with STEM imaging. For elemental mapping, the sample holder was tilted 17.0° towards the detector for better signal-to-noise ratio and the EDS maps were acquired in the range of 0 to 40 keV. The K α ₁ emission line was chosen for the composition of the colour map of the elements, Rh at 20.217 keV and Ti at 4.508 keV. The as-prepared colloidal samples were isolated by centrifugation, dried under vacuum and analysed by X-ray photoelectron spectroscopy (XPS) using Al-K α radiation and a Scientia Omicron hemispherical analyser. Adventitious C 1s (284.8 eV) was used as a reference. Textural characterization was performed from low-temperature N₂ adsorption-desorption isotherms (Tristar Kr 3020, Micromeritics). Prior to the measurements, the samples were degassed at 120 °C under vacuum for 12 h. The specific surface area, S_{BET} was determined by BET (Brunauer, Emmett and Teller) multipoint technique.⁴¹ The total pore volume, V_p, was calculated at the maximal adsorption point (p/p₀ = 0.98 – 0.99). The pore size distribution by volume (PSDV) was computed through the self-consistent regularization under non-negative conditions of the pore size distribution function, f(R_p) > 0 and at the regularization parameter $\alpha = 0.01$. The method allows us to estimate the contributions of different pore types based on their size: micro- (V_{micro} at R_p < 1 nm), meso- (V_{meso} at 1 nm < R_p < 25 nm) and macropores (V_{macro}, R_p > 25 nm). The mathematical aspects are discussed

particularly in the papers.⁴²⁻⁴⁵ The fractality was determined from the Frenkel-Halsey-Hill (FHH) method involving the isotherm's adsorption branch within $p/p_0 < 0.8$. The fractal dimension D_s was calculated from the plot corresponding to the equation $\ln(V/V_0) = (D_s - 3) \cdot \ln[\ln(p_0/p)] + const$, where V and V_0 are the adsorbed volume of N_2 , the saturation volume of adsorbed N_2 , respectively; p and p_0 are the equilibrium and saturation pressure of nitrogen adsorbed, respectively.

The electronic properties of Rh impregnated on TiO_2 were measured by UV-Vis diffuse reflectance spectroscopy using a Shimadzu UV2100 equipped with an integration sphere accessory. Powder samples were packed into the sample holder and measured against $BaSO_4$ as standard.

1.5 Photocatalytic H_2 production experiments

In a reactor vessel, 10 mg of the corresponding catalyst were dissolved in 9 mL of deionized water and 1 mL of methanol. The mixture was sonicated for 30 s at 1000 W in order to disperse the catalyst and the solution was deaerated by bubbling argon with a stainless-steel needle during 20 minutes. After this time, the reactor was placed in the UV-LED reactor and periodic samples of the headspace analysed (H_2 , CO, CH_4 and CO_2 content) with the aid of a gastight syringe (100 μ L) in a GC equipped with TCD detector. The production of CO and CH_4 is negligible, but the overall production of CO_2 is about 1/3 of the production of H_2 , as a sub-product of methanol oxidation.

The relative photonic efficiency (ζ_r)⁴⁶ was estimated by using the Formula 3 below, which correlates the amount of H_2 produced, considering a $2e^-$ reaction, with the photon flux measured by the ferrioxalate actinometry.

$$\zeta_r(\%) = \frac{2n_{H_2 \text{ produced}} (\mu\text{mol min}^{-1})}{n_{\text{photons}} (\text{min}^{-1})} \times 100 \quad (3)$$

2. Results and discussion

2.1 UV-LED Lamp reactor and actinometry

In this work it was used a home-made UV-LED reactor as a light source which is low cost and has low energy consumption in comparison to other types of light sources and high intense monochromatic emission.^{47, 48} Ferrioxalate actinometry was used to probe the photon flux of the UV-LED reactor and in Figure 2 is shown the UV-Vis spectra after/before 5 minutes irradiation in both wavelengths studied here. Using the absorbance value at 510 nm it was estimated the photon flux of each UV-LED strip, as shown in Table 1.

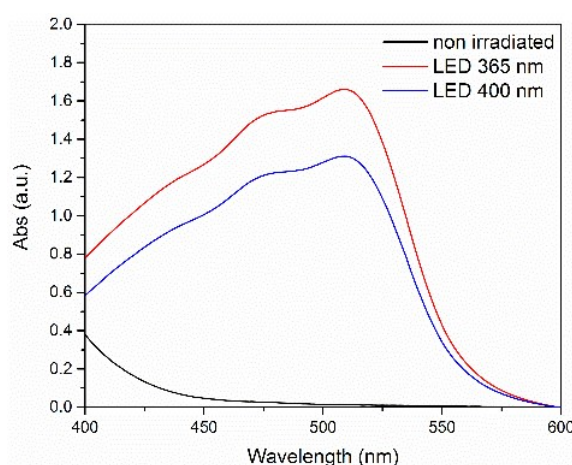


Figure 2. UV-Vis spectra of ferrioxalate actinometry, before (black line) and after irradiation (red line), using 365 nm UV-LED and (blue line) using 400 nm UV-LED.

Table 1. Measured photon flux of each UV-LED assembly.

Lamp Reactor	ΔA	Photon flux (photons $\text{min}^{-1} \times 10^{-6}$)
365 nm	1.56	2.22
400 nm	1.25	2.06

2.2 Rh-TiO₂ characterization

The average size distribution and the morphology of the Rh nanoparticles was probed by conventional TEM (Figure 3). As expected, the chemical reduction of Rh by NaBH₄ afforded to very small spherical nanoparticles with a narrow size distribution. The cubic and octahedral nanoparticles were prepared by polyol solvolysis at high temperature using Br⁻ ions and citrate as shape inducers. The

1
2
3 mean size and distribution of the nanoparticles are summarized in the Table 2. RhNC were measured diagonally meanwhile RhOh were measured by the longest length of the nanoparticles.
4
5
6
7

8
9 As the statistical analysis of the Rh nanoparticles size distribution has shown (Figure S2), all
10 three samples are characterized by a strict tendency in the average diameter growth together with the
11 standard deviation in the RhNP – RhNC – RhOh series. This, in turn, speaks for a less dispersed
12 character of the spherical nanoparticles – the standard deviations (SDs) for RhNC and RhOh are as
13 higher as ca. 2 and 4 in comparison to SD for RhNP. The enlargement of the interquartile range (0.4875,
14 0.9563, 2.47 for RhNP, RhNC and RhOh, respectively) and normal character for non-spherical particles
15 may favour a view that polyol affected synthesis procedures for RhNC and RhOh occur stochastically,
16 i.e., in both cases, the formation of larger nanoparticles required more time to achieve the equilibrium.
17 The reduction in the presence of NaBH₄ for RhNP could be controlled kinetically resulting in enhanced
18 selectivity with the set nanoparticles size. Taking a closer look at the distribution's profiles, RhNC and
19 RhOh demonstrate normality validated by the D'Agostino-Pearson test, revealing $p_{D-P} > 0.05$ (0.275
20 and 0.068, respectively). Contrastingly, RhNP has not passed the normality test at $p_{D-P} \ll 0.05$ (Figure
21 S2).
22
23
24
25
26
27
28
29
30
31
32
33
34
35
36
37
38
39
40
41
42
43
44
45
46
47
48
49
50
51
52
53
54
55
56
57
58
59
60

After impregnation on TiO₂, the catalysts were characterized by HRTEM as shown in Figure
3. For RhNC and RhOh it was possible to measure the lattice spacing of the Rh and TiO₂, Figure 3e, f,
and the measured distances by FFT are in accordance to fcc structure of Rh. The lattice planes of RhNC
and RhOh shows contributions of (200) and (111) planes at 0.20 nm and 0.23 nm, respectively, which
are close to the previously reported data.⁴⁹ Since the RhNP were on top of TiO₂, the FFT results could
not be assigned. Also, the catalysts were analysed by STEM-EDS and it was confirmed the elemental
composition of the nanoparticles on the surface of TiO₂ (Figure 4). The heterojunction of Rh and TiO₂
was investigated by UV-vis DRS (Tauc plots in Figure S3). The influence of ionic liquids on TiO₂ was
investigated by impregnation of [BMIm.OAc] on TiO₂. It was observed that the presence of IL shifted
down the bandgap value. The calculated direct band gaps of impregnated Rh materials showed to have
increased values in comparison with pristine TiO₂ (Table 2). Upon increasing the metal content

impregnated on TiO₂, the bandgap shifted to higher values. This behaviour is probably due to the overlap in the absorption spectra of the Rh colloids, ionic liquids, and TiO₂.

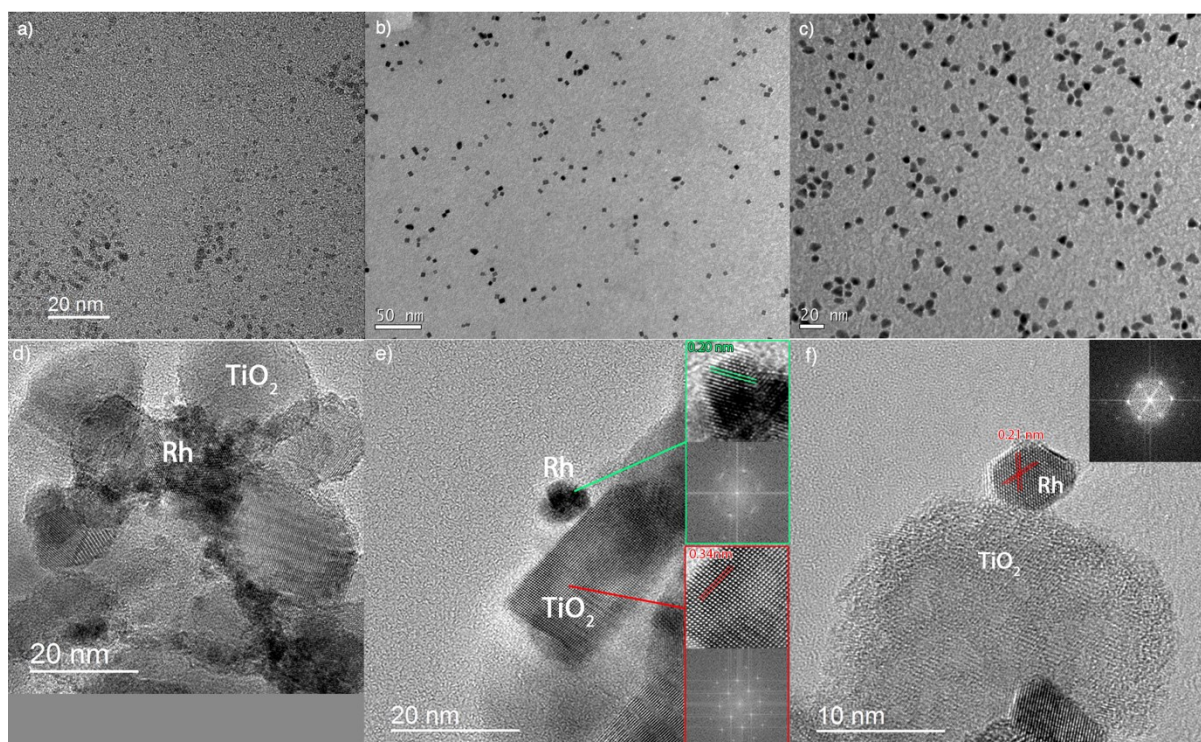
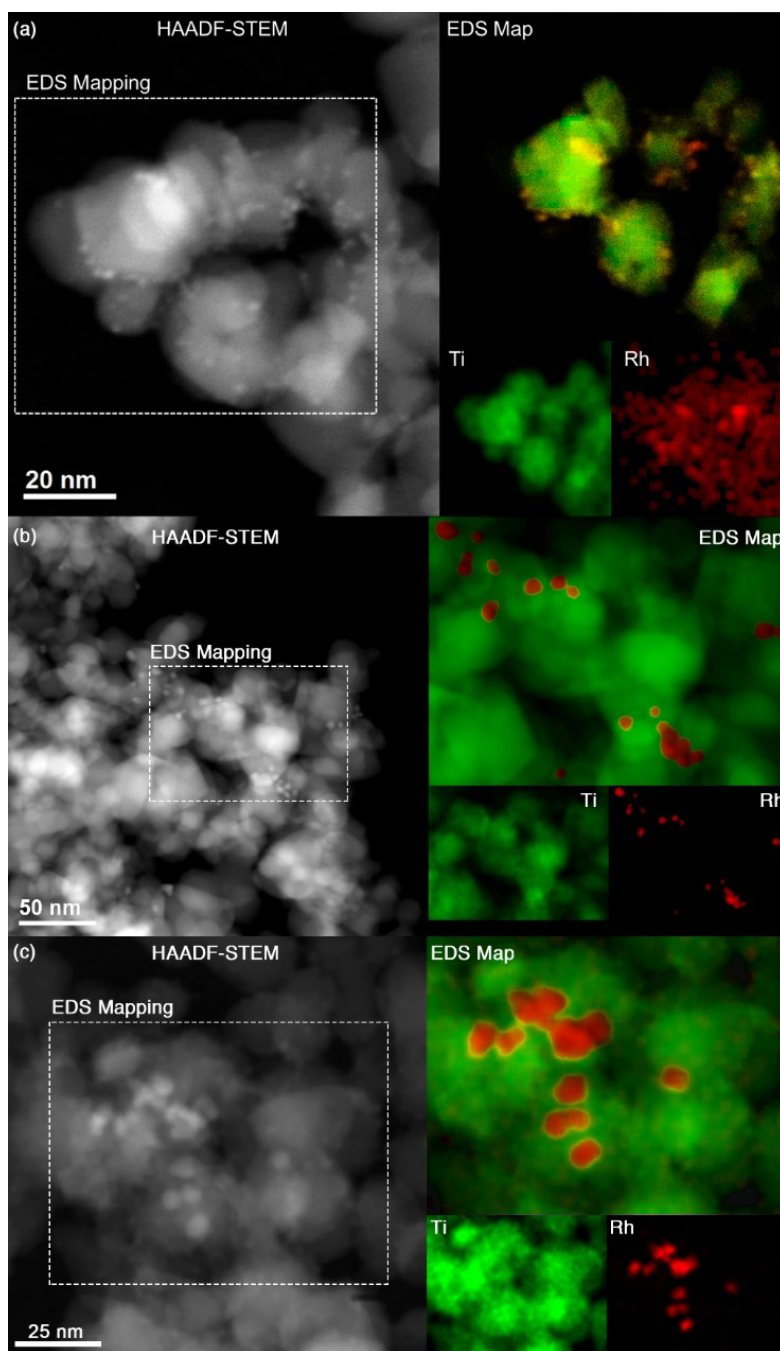


Figure 3. TEM image of colloidal a) RhNP, b) RhNC, c) RhOh and HRTEM images of d) RhNP, e) RhNC showing the (200) atomic planes and corresponding FFT for Rh (green box) and TiO₂ (red box) and f) RhOh a single RhOh nanoparticle in TiO₂ showing the (111) atomic planes of Rh and corresponding FFT (inset).

Table 2. Physico-chemical characterisation of the catalysts.

System	TEM Size (nm)	Rh amount FAAS (%)	Ratio Rh ⁰ /Rh ^{+x} (%) ^a	Bandgap (eV) ^b
TiO ₂	-	-	-	3.20
RhNP	1.6 ± 0.4	0.24	38,8	3.58
RhNC	5.7 ± 0.7	0.09	63,2	3.40 ^b
RhOh	8.4 ± 1.7	0.11	78,1	3.47

^a Determined by XPS analysis of unsupported nanoparticles. ^b Direct bandgap determined by linear extrapolation of Tauc plots. ^c Increasing the metal content to 0.56 % (w/w) shifted the direct bandgap to 3.76 eV.



View Article Online
DOI: 10.1039/D0NJ02419H

Figure 4. HAADF-STEM/EDS of a) RhNP, b) RhNC and c) RhOh, the inset presents the EDS mapping and individual contribution of Ti and Rh (colorized images).

The electronic state of Rh NPs synthesized were measured by XPS and the Rh 3d region are shown in Figure 5 and in Table 2 (the survey spectrum can be found in the ESI, Figure S4). The data were acquired on the as-prepared non-supported nanoparticles, after isolation by centrifugation and washing with DI H₂O, due to the low Rh loading on the final catalyst. As the nanoparticles were in

different sizes, the Rh 3d region shows an increase in the Rh^{+x} contribution in the smaller particles as already observed by others.^{34, 50, 51} Two contributions from Rh^0 and Rh^{+x} were used for the deconvolution of the data with peaks in 307.0 and 309.2 eV, respectively.

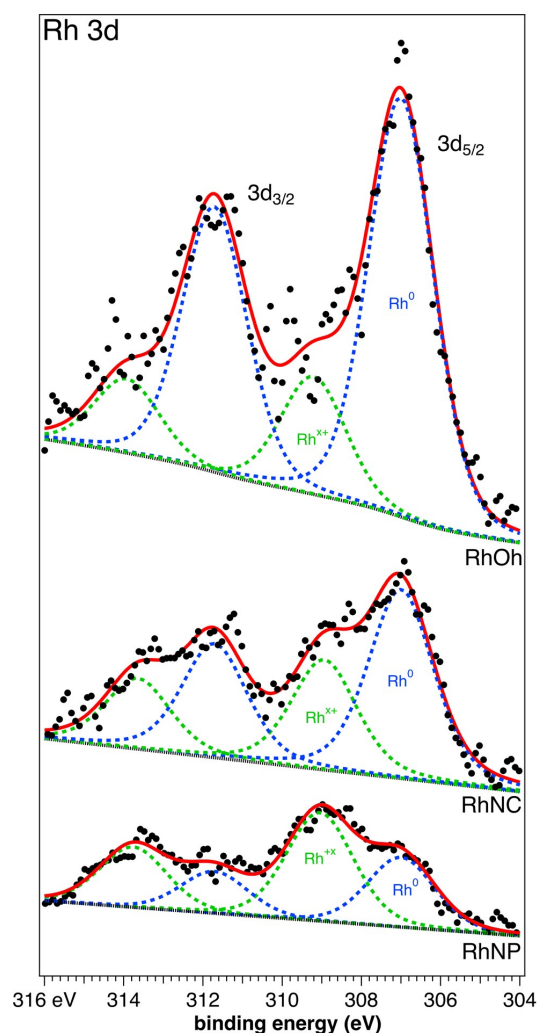


Figure 5. XPS of Rh 3d region of the nanoparticles synthesized in our work, highlighting the presence of both Rh^0 and Rh^{+x} contributions centred in 307.0 and 309.2 eV, respectively.

The N_2 adsorption/desorption was evaluated for the catalysts synthesized in this work and showed similar behaviour for all catalysts Figure 6a. Specific surface area, S_{BET} was determined from the standard BET method and the total pore volume, V_p was calculated at $p/p_0 = 0.98-0.99$. The pore radius analysis, Figure 6b, indicated a decreased porosity that is reflected in lowered total pore volume and augmented average pore radius in RhNC and RhOh, as compared to RhNP. Hierarchically,

the key alteration in the morphology occurs with aggregates and agglomerates of aggregates one can see this by elevated values of the fractal dimensions – from 2.44 (RhNP) up to 2.51 and 2.52 (RhNC and RhOh, respectively, shown in Figure S5). The rearrangement of the aggregated structure is especially visible comparing RhNC and RhOh, while at lower V_p (RhNC) the mesoporosity is maintained, as in case of RhOh, i.e. the contributions of meso- and macropores are almost equal, whereas the size of TiO₂ primary particles did not undergo any alteration. Notice, that RhNC and RhOh feature in slightly enlarged rhodium nanoparticles giving an additional fraction despite their lower concentration in both hybrid catalysts in comparison to RhNP. Hence, a complex introduction of modifiers (1) and magnified Rh nanoparticles (2) leads to the decrease of empty volume (V_{em}) related to the true (ρ_0) and bulk (ρ_b) density of the powders: $V_{em} = 1/\rho_b - 1/\rho_0$, where the value of ρ_b undergoes increase.

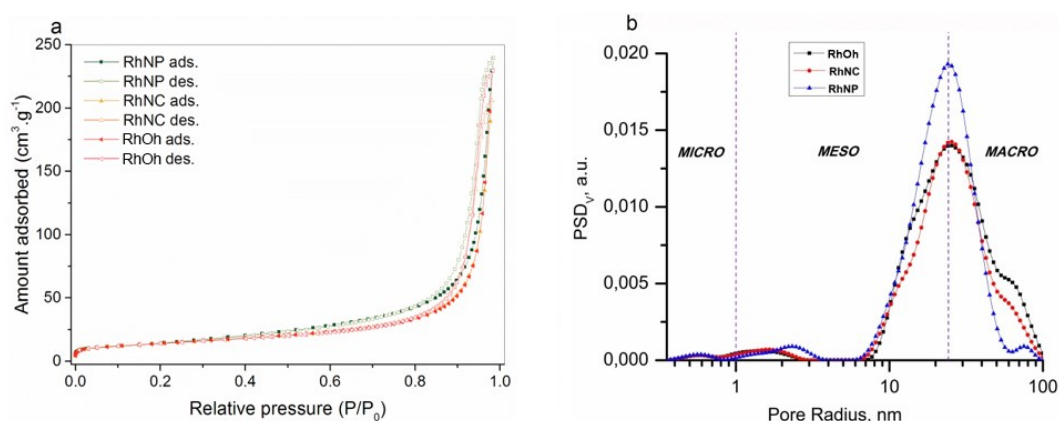


Figure 6. a) N₂ adsorption/desorption isotherms and b) the pore size distribution by volume of the catalysts synthesized in this work.

Table 3. Textural characteristics of RhOh, RhNC and RhNP materials.

Sample	S _{BET} (m ² /g)	V _p (cm ³ /g)	V _{micro} /V _p (%)	V _{meso} /V _p (%)	V _{macro} /V _p (%)	R _p , (nm)	D _s
RhOh	50	0.355	1.3	52.1	46.6	53	2.52
RhNC	50	0.317	1.5	54.3	44.3	49	2.51
RhNP	54	0.371	1.0	64.0	35.0	34	2.44

2.3 Photocatalytic H₂ production experiments.

View Article Online
DOI: 10.1039/D0NJ02419H

The H₂ production reactions were carried out at room temperature using a 10% methanol aqueous solution (10 mL) and 1.0 g L⁻¹ of catalyst concentration during a period of five hours (The kinetics of H₂ production of all catalysts is shown in Figure 7). In the absence of MeOH the H₂ production was negligible; this is due to the methanol is scavenging holes decreasing the recombination, but a part of H₂ is coming from photoreforming (coming from photooxidation) of methanol. A 25-fold increase in H₂ formation by the spherical nanoparticles in comparison with pristine TiO₂ and the colloidal nanoparticles was observed (up to 23.0 mmol g⁻¹ of H₂ after 5 hours of reaction). Since RhNP was shown to have the smallest size among the Rh nanoparticles applied in this study, the number of particles on the surface of TiO₂ presents a higher number of active sites for the generation of H₂.

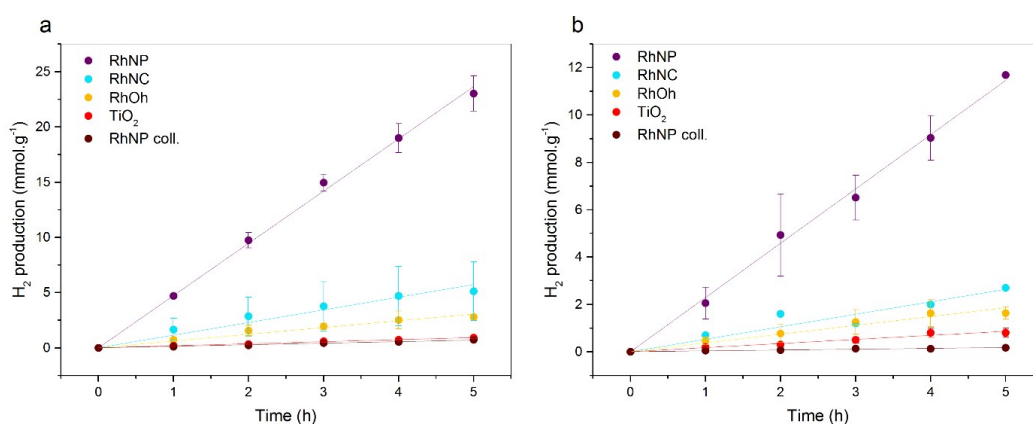


Figure 7. Kinetic profiles of H₂ production over gram of catalyst per time, (a) at 365 nm irradiation and (b) at 400 nm irradiation.

As shown in Figure 8, the wavelength influence in the H₂ production can be also assessed upon the comparison of the H₂ production per gram of catalyst. The production per gram of catalyst of RhNP at 365 nm irradiation figure among the best results so far in these conditions (using commercial TiO₂ and methanol as sacrificial reagent).⁵² In comparison with other Rh catalysts under irradiation at the same region, our result is around 5 times better than previous reported, when normalized by catalyst loading.⁵³ A comparison of other Rh-based catalysts can be found on Table S1, but the direct

comparison is difficult since it was used different conditions, such as choice of support, sacrificial reagent and irradiation wavelength/source.

Pristine TiO_2 showed the same production after five hours of reaction independent of the incident wavelength. However, by using the colloidal RhNP, it is clear that activation of the metallic surface upon irradiation at shorter wavelengths occurs. For non-plasmonic metals, interband transitions play a significant role in the light-activated catalysis.⁵⁴ Excitation of *d*-band electrons can be absorbed by the support and contribute to the generation of hot electrons and holes.⁵⁵ The excitation of *d*-band electrons can also interact with the LUMO of the adsorbed species at the surface of the Rh nanoparticles, therefore, promoting the reaction.

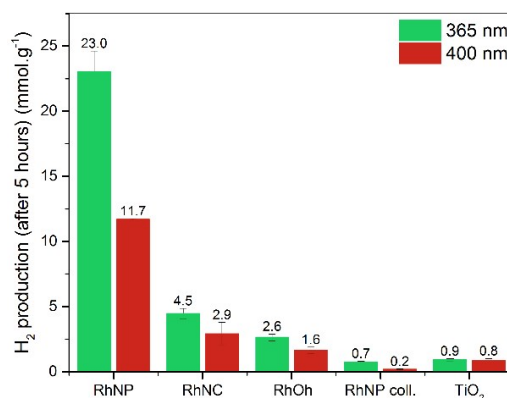


Figure 8. Normalised H_2 production per gram of catalyst after 5 hours of reaction.

Although Rh nanocubes can exhibit localized surface plasmon resonance bands (LSPR),⁵⁶ the position of the plasmonic band depends on size⁵⁷ whereas the size of RhNC is much smaller than the Rh nanocubes which exhibit LSPR in the emission wavelengths of LED used in this work. The position of the interband transitions of the Rh nanoparticles studied here overlaps with the absorption of UV light by TiO_2 . Therefore, a dual-excitation pathway can lead to a better efficiency in the generation of electron-hole pairs on TiO_2 ,⁵⁸ culminating with a strong synergetic effect in the catalysts. Upon preparing a catalyst with a higher amount of RhNC, the activity did not increase linearly (See Figure S6). This fact can be explained by an RhNC blocking out effect over TiO_2 light absorption that leads to lower activities.⁵⁹ The irradiation of a 300 W Xe lamp without an UV bandpass filter, commonly

employed in solar simulation photocatalysis, didn't affect the catalyst performance as tested using RhNP (the comparison of kinetics over 4 hour reaction is shown in Figure S7). Therefore, we estimated that using visible light (> 400 nm) would not increase the H₂ production, as observed by comparison of 365 nm and 400 nm LED lamps.

The specific rate of H₂ production was calculated after measuring the average size of the nanoparticles by TEM analysis, the rate of H₂ production and, the amount of Rh on TiO₂ determined by FAAS, assuming that the surface in contact with TiO₂ was proportional for all samples,⁶⁰ (Table 4 and SI for details). This approximation is similar to already estimated for colloidal nanoparticles in heterogeneous reactions⁶¹. The specific rate of H₂ production was 3.0 μmol h⁻¹ m⁻² for pristine TiO₂ and 0.95 μmol h⁻¹ m⁻² for colloidal Rh at 365 nm, and 3.2 μmol h⁻¹ m⁻² and 0.19 μmol h⁻¹ m⁻² at 400 nm, respectively. Under these conditions, there is no dependency upon the incident wavelength of the UV-LED lamp using only TiO₂ as a catalyst. However, when Rh is impregnated on TiO₂ the H₂ production is highly dependent on the incident wavelength. For RhNP, the activity at 365 nm had a two-fold enhancement in comparison with the 400 nm irradiation. For RhNC activity was about a three-fold increased, meanwhile RhOh, showed to be not very dependent upon the incident wavelength, which constitutes evidence of a better activity in the presence of [100] faceted NPs. Spherical (cuboctahedra) nanoparticles have both [111] and [100] facets on the surface,³⁷ and therefore showed an increase in activity for H₂ production. RhNC, which is composed mainly of [100] exposed facets,³⁷ the activity was even higher at shorter wavelengths. Finally, for RhOh, which surface is mainly composed of [111] facets, activity remained almost unaltered. The higher activity of the RhNP, among the catalysts tested, could be associated with two mainly factors: 1) the higher concentration of Rh impregnated on TiO₂, and 2) the higher surface-to-volume ratio in comparison with the other Rh nanoparticles synthesised in this study. The stability of the catalysts before the reaction was assessed by conventional TEM, using both TiO₂-supported and unsupported RhNP (spheres) as shown in Figure S8. Although is difficult to have a good statistical counting on supported nanoparticles, is possible to observe that the size remains unaltered after the catalytic cycle, which is also true when using unsupported nanoparticles.

Table 4. Specific rate of H₂ production and relative photonic efficiency, ζ_r , of the catalysts upon different incident wavelengths.

System	Specific Rate (mmol h ⁻¹ m ⁻²) ^a		ζ_r (%)	
	365 nm	400 nm	365 nm	400 nm
TiO ₂	3.0x10 ^{-3(b)}	3.2x10 ^{-3(b)}	2.7	2.7
RhNP	13.5	5.6	73.8	30.6
RhNC	22.4	7.5	26.1	8.7
RhOh	7.9	5.2	9.2	6.2
RhNP ^c	9.5x10 ⁻⁴	1.9x10 ⁻⁴	0.08	0.02

^aValues were determined by the linear fit of the slope of H₂ production kinetics in a 5-hour reaction at room temperature, the reported data is an average of at least three independent experiments. ^bSpecific Rate calculated using BET surface area value (56 m² g⁻¹). ^cColloidal nanoparticles.

Upon normalising the average activity by surface area for the amount of Rh in each sample, it is possible to observe a higher activity of RhNC. The observed activity trend of RhNC > RhNP > RhOh is similar with earlier reports on Pd nanocubes and octahedra with different sizes for H₂ production in aqueous methanol.⁶² The higher activity of the RhNC might be due to the higher surface energy of the Rh nanoparticles, in comparison with other metals such as Au, Pt, and Pd, regardless their shape.⁶³ The higher activity observed for the RhNC and RhNP could be an effect of the presence of imidazolium ionic liquids in its preparation. It is well known that the interaction of imidazolium cations with metal nanoparticle surface could produce Metal-*N*-heterocyclic carbene species (M-NHC)⁶⁴⁻⁶⁶ and consequently different catalytic activities. To confirm the influence of IL in water photolysis, the RhOh catalyst was treated with [BMIm.OAc] and TGA analysis showed a 2 wt % in remained on TiO₂ (Figure S9). The small increase in activity after impregnation with the IL (Figure S10), can be explained by two different mechanisms: 1) the formation of Rh-NHC carbene species at the surface⁶⁵ and, 2) the interaction of the ionic pair with the TiO₂ surface which synergically shifts the bandgap.⁶⁷ The bandgap for the IL-doped RhOh also decreased from 3.47 to 3.44 eV, a difference of 0.03 eV, which is similar to the 0.05 eV difference when doping the TiO₂ with the IL. This result is evidence of the IL cation participation on the photocatalytic effect as observed before.⁶⁷

The ζ_r was determined and since the estimation was carried out using the same catalyst loading and the LED lamps in our study, an apparent quantum efficiency (Φ_{app}) was not used in this study. The results are compiled in Table 4. It can be noted that all Rh-impregnated catalysts showed better efficiency than pristine TiO₂. The high ζ_r values obtained in this work are also observable in the high H₂ production of all catalysts, in special the RhNP, which converted approximately ~74 % of photons to H₂. Similar ζ_r values for equivalent H₂ production has been observed before,⁶⁸ but referred as apparent quantum efficiency, Φ_{app} . The discussion of using Φ_{app} to heterogeneous photocatalysis can be found elsewhere.^{46, 69} Also, the reactor design may play a major role since the sample is irradiated in all directions minimizing the scattering effects of the powdered sample. The higher efficiency of the systems at lower wavelength is probably due to the better photon absorption by TiO₂ and, therefore a better charge transfer to the co-catalyst. TiO₂ exhibited the same ζ_r for both wavelengths, due to its absorption spectra in the UV region. In the case of RhOh, the ζ_r difference between the wavelengths is less evident, 9.2 % versus 6.2 % for 365 nm and 400 nm, respectively. This effect for Rh photocatalysis was also observed in the photodegradation of 4-chlorophenol by UV and Visible light.⁷⁰

3. Conclusions

The results presented in this paper show that the photocatalytic activity is directly related to the exposed facets of the Rh-cocatalyst and that can be tailored by the shape of MNPs. The H₂ production is among the best reported so far using UV LED lamps and commercial TiO₂. Despite using Rh as a cocatalyst, it was observed that a very low amount of impregnation (i.e. RhNP at 0.24 %) is enough to achieve a Hydrogen production of about 4.68 mmol h⁻¹ per gram of catalyst. A triple synergic effect of TiO₂, Rh nanoparticle and the ionic liquid was observed. The incident photon energy was also an important observation in this work. By only a few nanometres of difference in the UV-LED emission, an increase of about 30% in the H₂ production activity and ζ_r using spherical and cubic nanoparticles. The application of magic numbers approach to unveil the surface activity of the catalysts was essential to rationalize the morphological effects. All of these observations reveal a trend in the H₂ production of the exposed facets [100] > [111] on studied conditions. The hydrogen generation presented in this work

figure among the best reported so far for rhodium co-catalysts impregnated in TiO₂. Also, common LED strips can be used as a photon source for the production of hydrogen in aqueous methanolic solutions. This can be applied to different alcohols to seek a more environmentally friendly H₂ production. The electric energy demand for LED light sources shows good potential for sunlight powered systems with the aid of common photovoltaic cells.

Conflicts of interest

There are no conflicts to declare.

Acknowledgements

The authors are thankful for financial support from CAPES (158804/2017-01 and 001), FAPERGS (16/2552-0000 and 18/2551-0000561-4), CNPq (406260/2018-4, 406750/2016-5 and 465454/2014-3). We are grateful for the National Laboratory of Nanotechnology (LNNano-Campinas) under proposal TEM-24375 for the HRTEM analysis, the Central Laboratory of Electron Microscopy (LCME) at UFSC for the TEM analysis, the Laboratory of Atomic Spectrometry at IQ-UFRGS for the FAAS analysis and Prof. Claudio Radtke (UFRGS) for XPS experiments.

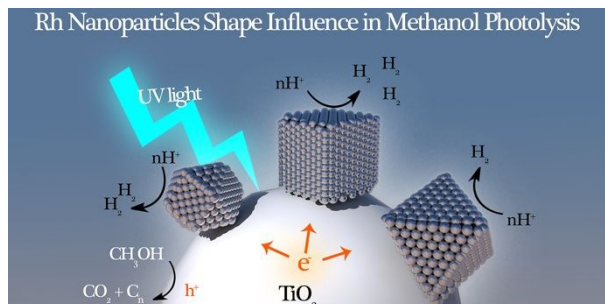
Notes and references

1. A. Fujishima and K. Honda, *Nature*, 1972, **238**, 37-38.
2. K. Hashimoto, H. Irie and A. Fujishima, *Jpn. J. Appl. Phys.*, 2005, **44**, 8269-8285.
3. G. R. Bamwenda, S. Tsubota, T. Nakamura and M. Haruta, *J. Photochem. Photobiol. A*, 1995, **89**, 177-189.
4. M. Ni, M. K. H. Leung, D. Y. C. Leung and K. Sumathy, *Renewable Sustainable Energy Rev.*, 2007, **11**, 401-425.
5. J. Yu, L. Qi and M. Jaroniec, *J. Phys. Chem. C*, 2010, **114**, 13118-13125.
6. L. Liu, H. Zhao, J. M. Andino and Y. Li, *ACS Catal.*, 2012, **2**, 1817-1828.
7. M. I. Qadir, M. Zanatta, E. S. Gil, H. K. Stassen, P. Gonçalves, B. A. D. Neto, P. E. N. de Souza and J. Dupont, *ChemSusChem*, 2019, **12**, 1011-1016.
8. J. Yu, J. Low, W. Xiao, P. Zhou and M. Jaroniec, *J. Am. Chem. Soc.*, 2014, **136**, 8839-8842.

- 1
2
3
4
5
6
7
8
9
10
11
12
13
14
15
16
17
18
19
20
21
22
23
24
25
26
27
28
29
30
31
32
33
34
35
36
37
38
39
40
41
42
43
44
45
46
47
48
49
50
51
52
53
54
55
56
57
58
59
60
9. H. Dong, G. Zeng, L. Tang, C. Fan, C. Zhang, X. He and Y. He, *Water Res.*, 2015, **79**, 128-146. View Article Online
DOI: 10.1039/C5WJ02419H
10. B. Sirota, J. Reyes-Cuellar, P. Kohli, L. Wang, M. E. McCarroll and S. M. Aouadi, *Thin Solid Films*, 2012, **520**, 6118-6123.
11. S. Sood, A. Umar, S. Kumar Mehta and S. Kumar Kansal, *Ceram. Int.*, 2015, **41**, 3355-3364.
12. D. M. Schultz and T. P. Yoon, *Science*, 2014, **343**, 1239176-1239176.
13. M. Oelgemoller, *Chem. Rev.*, 2016, **116**, 9664-9682.
14. W. K. Jo and R. J. Tayade, *Ind Eng Chem Res*, 2014, **53**, 2073-2084.
15. M. P. Languer, F. R. Scheffer, A. F. Feil, D. L. Baptista, P. Migowski, G. J. Machado, D. P. de Moraes, J. Dupont, S. R. Teixeira and D. E. Weibel, *Int. J. Hydrog. Energy*, 2013, **38**, 14440-14450.
16. R. V. Gonçalves, H. Wender, P. Migowski, A. F. Feil, D. Eberhardt, J. Boita, S. Khan, G. Machado, J. Dupont and S. R. Teixeira, *J. Phys. Chem. C*, 2017, **121**, 5855-5863.
17. T. N. Ravishankar, M. de O. Vaz, T. Ramakrishnappa, S. R. Teixeira, J. Dupont, R. K. Pai and G. Banuprakash, *J. Mater. Sci.*, 2018, **29**, 11132-11143.
18. S. Cao, J. Jiang, B. Zhu and J. Yu, *Phys. Chem. Chem. Phys.*, 2016, **18**, 19457-19463.
19. S. Fodor, G. Kovács, K. Hernádi, V. Danciu, L. Baia and Z. Pap, *Catal. Today*, 2017, **284**, 137-145.
20. H. Kotani, R. Hanazaki, K. Ohkubo, Y. Yamada and S. Fukuzumi, *Chem. Eur. J.*, 2011, **17**, 2777-2785.
21. Y.-F. Li and Z.-P. Liu, *J. Am. Chem. Soc.*, 2011, **133**, 15743-15752.
22. M. Luo, P. Lu, W. Yao, C. Huang, Q. Xu, Q. Wu, Y. Kuwahara and H. Yamashita, *ACS Appl. Mater. Interfaces*, 2016, **8**, 20667-20674.
23. M. Luo, W. Yao, C. Huang, Q. Wu and Q. Xu, *RSC Adv.*, 2015, **5**, 40892-40898.
24. T. S. Rodrigues, A. G. M. da Silva and P. H. C. Camargo, *J. Mater. Chem. A*, 2019, **7**, 5857-5874.
25. Y. Xia, X. Xia and H.-C. Peng, *J. Am. Chem. Soc.*, 2015, **137**, 7947-7966.
26. Y. Xia, Y. Xiong, B. Lim and S. E. Skrabalak, *Angew. Chem. Int. Ed.*, 2009, **48**, 60-103.
27. S. Xie, X. Y. Liu and Y. Xia, *Nano Res.*, 2015, **8**, 82-96.
28. Z. Huang, J. Gong and Z. Nie, *Acc. Chem. Res.*, 2019, **52**, 1125-1133.
29. H. Tada, *Dalton Trans.*, 2019, **48**, 6308-6313.
30. S. Cao, H. Li, Y. Li, B. Zhu and J. Yu, *ACS Sustainable Chem. Eng*, 2018, **6**, 6478-6487.
31. M. Luo, W. Yao, C. Huang, Q. Wu and Q. Xu, *J. Mater. Chem. A*, 2015, **3**, 13884-13891.

- 1
2
3
4
5
6
7
8
9
10
11
12
13
14
15
16
17
18
19
20
21
22
23
24
25
26
27
28
29
30
31
32
33
34
35
36
37
38
39
40
41
42
43
44
45
46
47
48
49
50
51
52
53
54
55
56
57
58
59
60
32. M. Luo, P. Lu, W. Yao, C. Huang, Q. Xu, Q. Wu, Y. Kuwahara and H. Yamashita, *ACS Appl. Mater. Interf.*, 2016, **8**, 20667-20674. View Article Online
DOI: 10.1039/C6JM02419H
33. F. Xue, C. Chen, W. Fu, M. Liu, C. Liu, P. Guo and S. Shen, *J. Phys. Chem. C*, 2018, **122**, 25165-25173.
34. Y. Zhang, D. A. J. M. Ligthart, X.-Y. Quek, L. Gao and E. J. M. Hensen, *Int. J. Hydrog. Energy*, 2014, **39**, 11537-11546.
35. T. Ikeda, A. Xiong, T. Yoshinaga, K. Maeda, K. Domen and T. Teranishi, *J. Phys. Chem. C*, 2012, **117**, 2467-2473.
36. A. P. Umpierre, E. de Jesus and J. Dupont, *ChemCatChem*, 2011, **3**, 1413-1418.
37. Y.-J. Wang, W. Long, L. Wang, R. Yuan, A. Ignaszak, B. Fang and D. P. Wilkinson, *Energy Environ. Sci.*, 2018, **11**, 258-275.
38. T. N. Nguyen, S. Kampouri, B. Valizadeh, W. Luo, D. Ongari, O. M. Planes, A. Züttel, B. Smit and K. C. Stylianou, *ACS Appl. Mater. Interfaces*, 2018, **10**, 30035-30039.
39. J. N. Demas, W. D. Bowman, E. F. Zalewski and R. A. Velapoldi, *J. Phys. Chem.*, 1981, **85**, 2766-2771.
40. C. Hubert, E. G. Bilé, A. Denicourt-Nowicki and A. Roucoux, *Green Chem.*, 2011, **13**.
41. P. A. Webb, C. Orr, R. W. Camp, J. P. Olivier and Y. S. Yunes, *Analytical Methods in Fine Particle Technology*, Micrometrics Instrument, 1st Ed. edn., 1997.
42. V. M. Gun'ko and D. D. Do, *Colloids Surf., A*, 2001, **193**, 71-83.
43. V. M. Gun'ko, *Appl. Surf. Sci.*, 2014, **307**, 444-454.
44. C. Nguyen and D. D. Do, *Langmuir*, 1999, **15**, 3608-3615.
45. C. Nguyen and D. D. Do, *Langmuir*, 2000, **16**, 7218-7222.
46. N. Serpone, *J. Photochem. Photobiol. A*, 1997, **104**, 1-12.
47. W.-K. Jo and R. J. Tayade, *Ind Eng Chem Res*, 2014, **53**, 2073-2084.
48. G. Matafonova and V. Batoev, *Water Res.*, 2018, **132**, 177-189.
49. A. J. Biacchi and R. E. Schaak, *ACS Nano*, 2015, **9**, 1707-1720.
50. V. Cimpeanu, M. Kočevár, V. I. Parvulescu and W. Leitner, *Angew. Chem. Int. Ed.*, 2009, **48**, 1085-1088.
51. M. E. Grass, Y. Zhang, D. R. Butcher, J. Y. Park, Y. Li, H. Bluhm, K. M. Bratlie, T. Zhang and G. A. Somorjai, *Angew. Chem. Int. Ed.*, 2008, **47**, 8893-8896.
52. R. Singh and S. Dutta, *Fuel*, 2018, **220**, 607-620.
53. T. H. Chiang, H. Lyu, T. Hisatomi, Y. Goto, T. Takata, M. Katayama, T. Minegishi and K. Domen, *ACS Catal.*, 2018, **8**, 2782-2788.

- 1
2
3
4
5
6
7
8
9
10
11
12
13
14
15
16
17
18
19
20
21
22
23
24
25
26
27
28
29
30
31
32
33
34
35
36
37
38
39
40
41
42
43
44
45
46
47
48
49
50
51
52
53
54
55
56
57
58
59
60
54. S. Sarina, H.-Y. Zhu, Q. Xiao, E. Jaatinen, J. Jia, Y. Huang, Z. Zheng and H. Wu, *Angew. Chem. Int. Ed.*, 2014, **53**, 2935-2940. View Article Online
DOI: 10.1039/C4NJ02419H
55. X. Zhang, Y. L. Chen, R.-S. Liu and D. P. Tsai, *Rep. Prog. Phys.*, 2013, **76**, 046401.
56. A. M. Watson, X. Zhang, R. Alcaraz de la Osa, J. M. Sanz, F. González, F. Moreno, G. Finkelstein, J. Liu and H. O. Everitt, *Nano Letters*, 2015, **15**, 1095-1100.
57. X. Zhang, P. Li, Á. Barreda, Y. Gutiérrez, F. González, F. Moreno, H. O. Everitt and J. Liu, *Nanoscale Horiz.*, 2016, **1**, 75-80.
58. X. Zhang, Y. L. Chen, R.-S. Liu and D. P. Tsai, *Rep. Prog. Phys.*, 2013, **76**, 046401.
59. T. Hisatomi, K. Maeda, K. Takanahe, J. Kubota and K. Domen, *J. Phys. Chem. C*, 2009, **113**, 21458-21466.
60. D. Faggion Junior, R. Haddad, F. Giroud, M. Holzinger, C. E. Maduro de Campos, J. J. S. Acuña, J. B. Domingos and S. Cosnier, *Nanoscale*, 2016, **8**, 10433-10440.
61. A. M. Signori, K. d. O. Santos, R. Eising, B. L. Albuquerque, F. C. Giacomelli and J. B. Domingos, *Langmuir*, 2010, **26**, 17772-17779.
62. F. Xue, C. Chen, W. Fu, M. Liu, C. Liu, P. Guo and S. Shen, *J. Phys. Chem. C*, 2018, **122**, 25165-25173.
63. S. Xie, X. Y. Liu and Y. Xia, *Nano Res.*, 2015, **8**, 82-96.
64. F. Bernardi, J. D. Scholten, G. H. Fecher, J. Dupont and J. Morais, *Chem. Phys. Lett.*, 2009, **479**, 113-116.
65. L. S. Ott, M. L. Cline, M. Deetlefs, K. R. Seddon and R. G. Finke, *J. Am. Chem. Soc.*, 2005, **127**, 5758-5759.
66. G. Chacón, J. Durand, I. Favier, E. Teuma and M. Gomez, *Fr.-Ukr. j. chem.*, 2016, **4**, 23-36.
67. H. Weber and B. Kirchner, *ChemSusChem*, 2016, **9**, 2505-2514.
68. W. Wang, S. Liu, L. Nie, B. Cheng and J. Yu, *Phys. Chem. Chem. Phys.*, 2013, **15**, 12033-12039.
69. A. Salinaro, A. V. Emeline, J. Zhao, H. Hidaka, V. K. Ryabchuk and N. Serpone, *Pure & Appl. Chem.*, 1999, **71**, 321-335.
70. L. Zang, W. Macyk, C. Lange, W. F. Maier, C. Antonius, D. Meissner and H. Kisch, *Chem. Eur. J.*, 2000, **6**, 379-384.

Table of Contents entry:View Article Online
DOI: 10.1039/D0NJ02419H

Rhodium nanoparticles with different morphology were synthesized to assess the influence of the exposed facet towards the hydrogen production in aqueous methanolic solution.